Deriving column-integrated thermospheric temperature with the N$_2$ Lyman–Birge–Hopfield (2,0) band

Clayton Cantrall[1], Tomoko Matsuo[1]

[1]Ann and H.J. Smead Department of Aerospace Engineering Sciences, University of Colorado Boulder, Boulder, CO, USA

Correspondence to: Clayton Cantrall (clayton.cantrall@colorado.edu)

Abstract. This paper presents a new technique to derive thermospheric temperature from space-based disk observations of far ultraviolet airglow. The technique, guided by findings from principal component analysis of synthetic daytime LBH disk emissions, uses a ratio of the emissions in two spectral channels that together span the Lyman–Birge–Hopfield (LBH) (2,0) band to determine the change in band shape with respect to a change in the rotational temperature of N$_2$. The benefits of the two-channel ratio approach include an elimination of representativeness error as absolute LBH intensities are not required in the derivation procedure and a reduced impact of systematic measurement error caused by variations in the instrumental performance across the LBH band system as a fully resolved system is also not required. It is shown that the derived temperature should, in general, be interpreted as a column-integrated property as opposed to a temperature at a specified altitude without utilization of a priori information of the thermospheric temperature profile. The two-channel ratio approach is demonstrated using NASA GOLD Level 1C disk emission data for the period of 2–8 November 2018 during which a small geomagnetic storm has occurred. Due to the lack of independent thermospheric temperature observations, the efficacy of the approach is validated through comparisons of the column-integrated temperature derived from GOLD Level 1C data with version 2 of the GOLD Level 2 temperature product as well as temperatures from first principle and empirical models. The storm-time thermospheric response manifested in the column-integrated temperature is also shown to corroborate well with hemispherically integrated Joule heating rates, ESA SWARM mass density at 460 km, and GOLD Level 2 column O/N$_2$ ratio.

1 Introduction

Remote sensing of Earth's far ultraviolet (FUV) airglow from space provides important insights into the energetics, dynamics, and composition of the upper atmosphere (Meier et al., 1991; Paxton et al., 2017). The N$_2$ Lyman-Birge-Hopfield (LBH) bands (~127-280 nm) are prominent daytime FUV airglow features that emanate from the lower to middle thermosphere (~120-200 km) upon the deposition of solar extreme ultraviolet radiation. Currently operating instruments measuring the LBH bands include the Thermosphere-Ionosphere-Mesosphere Energetics and Dynamics (TIMED) satellite's Global Ultraviolet Imager (GUVI) launched in 2001 (Christensen et al., 2003), the Defense Meteorological Satellite Program (DMSP) Special Sensor Ultraviolet Spectrographic Imager (SSUSI) launched in 2003 (Paxton et al., 2002), the Global-scale Observations of the Limb and Disk (GOLD) launched in 2018 (McClintock et al., 2020a), and the Ionospheric Connection Explorer's Far UltraViolet imaging spectrograph (FUV) launched in 2019 (Mende et al., 2017).

The utility of the LBH bands for probing thermospheric temperature was demonstrated by Aksnes et al. (2006) with limb observations by the Advanced Research and Global Observation Satellite's (ARGOS) High

Resolution Ionospheric and Thermospheric Spectrograph (HITS) instrument. Eastes et al. (2008) subsequently

40   showed that disk observations of LBH bands could be used for global monitoring of thermospheric temperature. These authors fit LBH laboratory spectra to observed emissions using an optimal estimation routine with varying parameters such as the N_2 rotational temperature, population rates of each vibrational band, N 149.3 nm emission intensity, O_2 photoabsorption, and background emission rates. GOLD became the first mission to provide a Level 2 data product of thermospheric temperature (T_{DISK}) attributed to around 160 km using LBH disk emissions between

45   ~132-162 nm with a similar retrieval implementation (Eastes et al., 2017). Thermospheric temperatures attributed to around 155 km have also been derived from TIMED GUVI observations (Zhang et al., 2019) using an intensity ratio between the (0,0) band and (1,0) band that the authors found to be quasi-linearly dependent on the N_2 rotational temperature.

        This paper presents a new technique to derive thermospheric temperature from FUV spectrographic

50   images. Section 2 provides background and exploration of the LBH temperature signal to motivate the new technique. The technique, unlike in past work, uses the ratio of two spectral channels that span a single LBH band to determine the change in band shape with respect to a change in the rotational temperature of N_2.
The technique has a straightforward implementation that is relatively unaffected by changes in instrument performance across the LBH band system and that does not require a forward model to reproduce the absolute

55   intensity of emissions as part of the temperature derivation procedure. These points are further elaborated in Section 3 along with a description of the technique. Section 3 also provides a discussion on potential error sources in the temperature derivation, and a rationale behind our interpretation of the derived temperature as a column-integrated property that we refer to as column-integrated thermospheric temperature, T_{ci}. Section 4 presents the demonstrative results of applying the technique to GOLD Level 1C radiance data for the period of 2–8 November 2018; during

60   which a small geomagnetic storm event has occurred. The derived thermospheric temperatures are compared to GOLD Level 2 T_{DISK} data product over the same period. Due to the lack of independent remotely sensed or in situ temperature measurements in the lower to middle thermosphere, the derived column-integrated temperatures are also compared to (1) synthetically generated column-integrated temperatures from model simulations by NOAA's Whole Atmosphere Model (WAM) (Akmaev et al., 2011), (2) Naval Research Lab Mass Spectrometer and

65   Incoherent Scatter Radar Extended (NRLMSISE-00) empirical model temperatures (Picone et al., 2002), and (3) observations of other thermospheric states, including GOLD Level 2 $\Sigma O/N_2$ data product (Correira et al., 2018) and mass density by ESA's SWARM constellation (Astafyeva et al., 2017) as well as hemispherically integrated Joule heating rates estimated from SuperDARN and ground-based magnetometer data by using the Assimilative Mapping of Geospace Observations (AMGeO) (AMGeO Collaboration, 2019; Matsuo, 2020).

70

2 Temperature Signal in LBH Emissions

        The thermospheric temperature signal is present in the rotational structure of the LBH bands. In the case of N_2, the rotational temperature is equivalent to the ambient neutral temperature (Aksnes et al., 2006). In order to motivate the new technique to extract this signal from the N_2 LBH (2,0) band, this section presents results from

75   principal component analysis (PCA) performed on simulated LBH emissions. It is shown that PCA analysis helps

Atmospheric
Measurement
Techniques
Discussions

Open Access

EGU

quantify the amplitude and signal-to-noise ratio (SNR) of this temperature signal in disk LBH emission data. Synthetic LBH emission data are generated by applying forward modeling explained in Section 2.1 to WAM simulation results for the period of 2–8 November 2018. WAM simulation experiments are executed with solar and geomagnetic forcing conditions specified according to the actual values of the F10.7, Kp, and hemispheric power

80 indices, solar wind velocities and densities, and interplanetary magnetic fields. Section 2.1 discusses forward modeling of LBH emissions and Section 2.2 presents the PCA results.

2.1 Forward Modeling of LBH Emissions

The forward model used to produce synthetic LBH emissions is built with the Global Airglow Model (GLOW)

85 (GLOW) and a radiative transfer model (Solomon, 2017). GLOW computes LBH volume emission rates as a function of altitude that are input into the radiative transfer model to produce line-of-sight emissions of the LBH band system. The two primary mechanisms generating LBH emissions are direct excitation from the N_2 ground state by photoelectron impact and radiative and collisional cascading between the singlet states (Eastes et al., 2000a). GLOW currently does not consider cascading effects for the LBH vibrational states (Solomon, 2017). Eastes et al.

90 (2000b) showed that cascading increases the total LBH emission by a factor of ~1.6. The primary extinction source of LBH emissions is O_2 photoabsorption, computed line-by-line in the radiative transfer model.

The most important component of the forward model for the purposes of deriving thermospheric temperatures is the LBH vibrational-rotational band model (Budzien et al., 2001). The band model is essentially a look-up table of laboratory LBH spectra that specifies, for a given temperature, a unique spectrum for the upper

95 vibrational states v'=0–9 of N_2. In the current implementation of the forward model, the v'=0–9 vibrational population rates are defined by a Franck–Condon based theoretical model and are held constant (Ajello et al., 1985; Ajello et al., 2020). Ajello et al. (1985) states that significant deviations from a Franck–Condon factor distribution can occur in planetary dayglow or aurora due to the energy distribution of the electron flux, and that excitation thresholding should be included in airglow models to accurately reproduce LBH band intensity. However, as

100 discussed in the following section, absolute band intensity is not needed to extract the N_2 rotational temperature.

2.2 PCA of Simulated LBH Emissions

PCA is a data reduction technique that is useful for identifying the dominant orthogonal modes of variability from data. PCA is applied here using eigenvalue decomposition on aggregated data sets of simulated

105 emissions of the LBH band system, I_{LBH}^s, during 2–8 November 2018 for a total of 8.1×10^4 samples. The useful results of PCA for this investigation are a set of eigenvectors (principal components), $\boldsymbol{v}$, that describe the mode of variability with associated eigenvalues, σ. Suppose that $\boldsymbol{v}$ is time-invariant and time-dependent coefficients, $\boldsymbol{c}$, represent the amplitude of the mode for each disk emission sample at a given time, where the total variance of $\boldsymbol{c}$ matches σ^2 for that mode.

110 Figure 1 shows the mean of simulated LBH radiance, $\overline{I_{LBH}^s}$, between 138–162 nm with a spectral sampling of 0.04 nm along with the first two leading modes of variability in the spectrum, $\boldsymbol{v}_B$ and $\boldsymbol{v}_T$, scaled by their eigenvalues or total standard deviations, σ_B and σ_T. The leading mode $\boldsymbol{v}_B$ is identified as the overall scaling of the

Atmospheric
Measurement
Techniques
Discussions

LBH intensity due to changes in solar and geomagnetic conditions, solar zenith angle (SZA), and emission angle. The value of $\sigma_B{}^2$ suggests that this mode accounts for 98.3% of the total variability in the simulated LBH spectra.

115 The second leading mode $\boldsymbol{v}_T$ is identified as the temperature signal (as explained later). According to the value of $\sigma_T{}^2$ this secondary mode accounts for 1.6% of the total variability in the simulated LBH spectra and is just 3% of the intensity of an LBH band. The correlation coefficient, R, between time-dependent coefficients for this temperature mode $\boldsymbol{c}_T$ and the simulated WAM temperatures at 160 km altitude over the course of 2–8 November 2018 is 0.68. Together these two principal components account for 99.9% of the variability in the simulated LBH

120 spectra. Figure 1 highlights that variability of the simulated LBH disk emission spectra can be represented in a small number of degrees of freedom (i.e., there is a significant amount of redundant information) and that the temperature signal is considerably weaker than the overall LBH intensity.

Figure 2 focuses on the LBH (2,0) band from the LBH band system shown in Fig. 1. Compared to the other LBH bands the (2,0) band is relatively bright and is isolated from the even brighter O emissions at 130.4 nm and

125 135.6 nm and the N emission at 149.3 nm (not shown in Fig. 1). Figure 2 shows $\boldsymbol{v}_T$ scaled by σ_T along with the amplitude of shot noise, $\sqrt{I^S_{LBH_{2,0}}}$. The magnitude of temperature mode $\boldsymbol{v}_T$ is less than the level of shot noise (SNR≈0.35), underscoring the need for denoising approaches to detect the temperature signal with sufficient SNR. A simple way to improve SNR, at the cost of spectral or spatial resolution, is with binning.

The temperature signal in LBH emissions manifests as the second leading mode of emission variability as

130 is apparent in the morphological shape of $\boldsymbol{v}_T$ displayed in Fig. 2. As the rotational temperature of N_2 increases there is an effective skewing of the LBH (2,0) band to longer wavelengths. The close inspection of $\boldsymbol{v}_T$ indicates that LBH (2,0) band emissions at wavelengths above 138.58 nm are positively correlated with temperature while those below are negatively correlated. Emissions at 138.58 nm are not affected by temperature variability so have zero amplitude in $\boldsymbol{v}_T$. This observation substantiates an approach of binning the LBH (2,0) band into two channels using 138.58 nm

135 as a boundary to preserve how the temperature signal manifests in the LBH emission's morphological shape. Channel A is defined as the sum of all wavelengths negatively correlated with temperature ($\sum_{\lambda=138.0}^{138.56} I_\lambda$), and channel B contains all wavelengths positively correlated with temperature ($\sum_{\lambda=138.56}^{139.2} I_\lambda$). The ratio B/A is a linear function of temperature. A similar two-channel ratio approach was adopted in Cantrall et al. (2019) for testing the feasibility of assimilating GOLD Level 1C data into the WAM but a justification of such an approach was not

140 provided.

In this study, the LBH (2,0) band is sampled at 0.04 nm resulting in 30 bins over 138.0–139.2 nm. Binning these 30 bins into two channels improves the SNR by a factor of about 4 from 0.35 to 1.4. While this SNR is still low, the temperature signal in the LBH (2,0) band is now above the shot noise level. The results from PCA of simulated data of LBH disk emissions suggest that the ratio of the two spectral channels A and B that span a single

145 LBH band (2,0) as defined above is sufficient to determine the change in the band shape related to temperature variation while improving the SNR of the temperature signal in LBH emissions.

3 Determination of Column-integrated Temperature from LBH (2,0) Band

This section presents the procedure to determine column-integrated thermospheric temperature, T_{ci}, from the N_2

150   rotational structure observed in top-of-atmosphere LBH emissions using the ratio of two channels that together span

the LBH (2,0) band as motivated in Section 2. Section 3.1 explains the procedure step by step, which is followed by

a discussion on potential error sources of T_{ci} in Section 3.2 and some analysis in Section 3.3 that supports the

interpretation of T_{ci} as a column-integrated temperature rather than a temperature attributed to a specific altitude.

155   **3.1 Procedure**

The procedure consists of four steps as follows:

1. Generate synthetic data of spectrally resolved LBH (2,0) band emissions for a range of
    temperature using the vibrational-rotational band model.

2. Apply an instrument model on the band model spectra data to calibrate for the instrument's

160   wavelength resolution and wavelength registration.

3. Bin the band model spectra data into channels A and B. Tabulate the relationship of B/A ratio to
    temperature as a look-up table.

4. Compute B/A ratio on observations of the LBH (2,0) band and determine T_{ci} by linearly
    regressing observed B/A ratio on the predetermined relationship between B/A ratio and

165   temperature.

The two-channel ratio approach has a number of benefits, most importantly, it can limit the impact of the

following uncertainties: (1) uncertainty associated with LBH excitation and extinction processes that affect the

absolute intensity of each band, and (2) uncertainty associated with both the low SNR of the temperature signal and

instrument performance variations across the LBH band system (See Section 3.2). In this approach, a measurement

170   of a fully resolved LBH band system is not required to derive T_{ci} nor is a forward model to produce absolute LBH

intensity.

3.2 Sources of Error

In general, there are two categories of error associated with determining physical parameters from

175   observations: measurement error and representativeness error. Measurement error is the error associated with the

measuring device while representativeness error is the difference between the observation and the physical model's

representation of the observation (Rodgers, 2000). There are measurement errors, both random and systematic, in

T_{ci}, but the two-channel ratio approach effectively eliminates representativeness error by not requiring a forward

model to produce absolute LBH band intensity. However, sources that cause relative differences in the channel

180   intensity other than temperature must also be quantified. For example, changes in the O_2 absorption cross section

over the band is the predominant source causing a 1.5% change in the relative intensity.

The predominant source of random measurement error that determines the precision in T_{ci} is shot noise. For

the case study with GOLD data, the T_{ci} random measurement error associated with GOLD observations is quantified

using Monte Carlo (MC) samples of simulated T_{ci} derivations considering the viewing conditions and instrument

185   performance (McClintock et al., 2020a,b). An estimate of the errors using MC samples is provided along with case
study results in Section 4.1.

Reliance on only a small bandwidth of LBH emissions simplifies uncertainty quantification of T_{ci}
derivations due to changes in instrument performance across the entire band system. There are still two dominant
sources of systematic bias in T_{ci} stemming from variations in the instrument's wavelength registration and

190   resolution. Figure 3 shows the bias in T_{ci} as a function of the error in the modeled wavelength registration and the
error in the wavelength resolution. It is apparent in Fig. 3 that a significant bias of about 50 K (5–10%) can occur if
the errors exceed a hundredth of a nanometer level for the wavelength registration and a tenth of a nanometer level
for wavelength resolution. A discussion on how these two sources of biases can be mitigated in deriving T_{ci} from
actual GOLD data is provided in Section 4.1.

195

3.3 Interpretation of Column-integrated Temperature

Interpretation of column-integrated temperature, T_{ci}, is addressed using synthetic LBH disk emission
observations generated by forward modeling WAM simulation results. The column-integrated temperature
computed from synthetic observations is hereafter denoted as T_{ci}^S to contrast to T_{ci}^G computed from GOLD LBH disk

200   emission data that is introduced later. To examine if T_{ci}^S can be attributed to a certain altitude we compare the WAM
altitude with a temperature that most closely matches T_{ci}^S, denoted as $z_{T_{ci}^S}$, to the altitude at the peak of the LBH
contribution function, $z_{\tau=1}$, where altitude where the LBH optical depth, τ, is unity. $z_{T_{ci}^S}$ and $z_{\tau=1}$ are computed over
the entire simulation period of 8–13 November 2018 and are shown in Fig. 4 with respect to solar SZA (black). For
low SZA, T_{ci}^S is shown to match most to WAM temperatures at altitudes, $z_{T_{ci}^S}$, that are 5–10 km higher (about 30–90

205   K hotter) than suggested by $z_{\tau=1}$. The gap between T_{ci}^S and temperature at $z_{\tau=1}$ becomes smaller as SZA increases.
This dependence of the difference between $z_{T_{ci}^S}$ and $z_{\tau=1}$ on SZA is explained by also considering the full-width-
half-max (FWHM) of the contribution function. Figure 4 shows that the contribution function peaks at about
153±2.5 km for SZA = 0° and about 185±10 km for SZA = 75°. The FWHM associated with these contribution
functions span about 120–180 km and about 160–250 km for the SZA = 0° and SZA = 75° cases, respectively

210   (Laskar et al., 2020). In the case of SZA = 0° the FWHM spans an altitude range in the lower thermosphere with the
steepest thermospheric temperature gradients resulting in a wide range of temperatures contributing to T_{ci}^S with a net
effect of a higher apparent temperature than that at $z_{\tau=1}$. As SZA increases the FWHM spans an altitude range
where the thermosphere becomes isothermal in the middle thermosphere resulting in a smaller range of temperatures
contributing to T_{ci}^S so the apparent temperature looks like the temperature at $z_{\tau=1}$.

215   Figure 4 furthermore reinforces that T_{ci} derived from the procedural steps specified in Section 3.1 is indeed
a column-integrated quantity, containing information from a larger altitude range of the lower-middle thermosphere
than just at $z_{\tau=1}$. Perhaps, T_{ci} can be justified to be attributed to $z_{\tau=1}$ when measurement and representativeness
errors exceed the gap between T_{ci} and the temperatures at $z_{\tau=1}$ at a given SZA. In general, specific altitude
attribution of T_{ci} requires additional a priori knowledge of the thermospheric temperature profile as demonstrated

Atmospheric
Measurement
Techniques

Open Access

EGU

Discussions

220   with T_{ci}^s derived from synthetic LBH disk emission observations wherein the a priori information is given by WAM
      simulations.

4 Case Study

      The two-channel ratio approach to derive the column-integrated temperature is demonstrated using NASA GOLD

225   Level 1C disk FUV emission data, T_{ci}^G, for the period of 2–8 November 2018 during which a small geomagnetic
      storm has occurred. Due to the lack of independent thermospheric temperature observations, the efficacy of this
      approach is validated through comparisons with GOLD Level 2 temperature product (T_{DISK}) and two-channel
      column-integrated temperatures computed from the synthetic observations using the WAM simulations (T_{ci}^s) as
      described in Section 2. T_{ci}^G is also compared to NRLMSISE-00 temperatures sampled at the altitude $z_{T_{ci}^s}$ based on the

230   SZA. This sampled MSIS temperature is denoted as T_{MSIS}. T_{ci}^G and T_{DISK} are equivalent variables only differing in
      the approach to determine column-integrated thermospheric temperature. Note that version 2 of T_{DISK} is used in
      these comparisons presented in the paper. The approach is further corroborated through comparisons of the storm-
      time changes of T_{ci}^G to hemispherically integrated Joule heating rates (Q_{JH}) estimated from SuperDARN and ground-
      based magnetometer data using AMGeO, ESA SWARM mass density measurements at 460 km ($\rho_{SWARM}^{460\ km}$) based on

235   calculation from precise orbit determinations using the Global Positioning System receivers on the spacecraft, and
      GOLD Level 2 $\Sigma O/N_2$ product ($\Sigma O/N_2^G$). Section 4.1 provides a description of the GOLD LBH Level 1C disk
      emission data used in the T_{ci}^G derivation, Section 4.2 presents results comparing T_{ci}^G with T_{DISK}, T_{MSIS}, and T_{ci}^s, and
      Section 4.3 presents results comparing the storm time response of T_{ci}^G with Q_{JH}, $\rho_{SWARM}^{460\ km}$, and $\Sigma O/N_2^G$. Table 1
      defines each of the variable symbols introduced above.

240

4.1 GOLD LBH Disk Emission Data

      GOLD observes the daytime FUV airglow from ~134–162 nm on Earth's disk between 6:10 and 20:10
      UTC from geostationary orbit at 47.5°W longitude (Eastes, 2020). GOLD produces a full disk image every ~30
      minutes at a spatial resolution of 125×125 km by alternating between scans of the Northern and Southern

245   hemisphere. The GOLD Level 1C radiance data with a spectral sampling of 0.04 nm are used to derive T_{ci}^G in this
      study. The GOLD Level 1C data is spatially binned by 2×2 (250×250 km spatial resolution) to improve the SNR by
      a factor of 2. Prior to deriving T_{ci}^G, efforts were made to reduce the impact of systematic biases that are present in
      version 2 of the GOLD Level 1C data product. Variations in wavelength registration along the GOLD detector are
      identified with the location of the LBH (2,0) band peak through fitting a log-normal distribution. Variations in

250   wavelength resolution are identified with the FWHM of the OI 135.6 doublet through fitting a 2-gaussian
      distribution. Corrections for wavelength registration and resolution are incorporated into Step 2 of the T_{ci} algorithm
      (see Section 3).

4.2 Comparing T_{ci}^G to T_{DISK}, T_{MSIS}, and T_{ci}^s

255   Figure 5 displays T_{ci}^G along with T_{DISK}, T_{MSIS}, and T_{ci}^s over Earth's disk viewed by GOLD for a five day window from 3–7 November 2018 at about 15 UTC, noon LT at the center of the disk (47.5°W, 0°N). A small geomagnetic storm has commenced the evening of November 4th and lasted through November 5th. T_{ci}^G agrees most with T_{MSIS} in the morphological temperature response to geomagnetic activity over the disk. There is also good agreement in the temperature morphology over the disk between T_{ci}^G and T_{ci}^s prior to the storm, but the storm-time

260 response simulated by WAM, as manifest in T_{ci}^s, shows considerably higher temperatures in the mid- and high-latitudes and a longer post-storm recovery time in comparison to T_{ci}^G as well as T_{MSIS}. T_{ci}^G and T_{DISK} show general agreement, particularly at low latitudes, but T_{DISK} exhibits a significant north-south temperature gradient and a relatively constant east-west gradient both of which are absent in T_{ci}^G as well as T_{MSIS}. Note that there is slight banding near the equator in T_{ci}^G where the southern and northern hemisphere scans meet that is likely due to

265 systematic errors (see Section 3.2) at the top and bottom edge of the detector that were not completely corrected.

    Figure 6 shows the root mean squared difference (RMSD) and mean bias difference (MBD) of T_{ci}^G from T_{DISK}, T_{MSIS}, and T_{ci}^s that is computed for a 5° latitudinal bin. In general, there is agreement of T_{ci}^G with T_{DISK}, T_{MSIS}, and T_{ci}^s at low latitudes as suggested by the RMSD and MBD. The consistent −25 K MBD at low latitudes for each paired difference, $T_{ci}^G - T_{DISK}$, $T_{ci}^G - T_{MSIS}$, and $T_{ci}^G - T_{ci}^s$, suggests that there is an overall bias in T_{ci}^G likely due to

270 wavelength registration and/or resolution errors. There are also small-scale fluctuations in MBD observed in each pair that suggests small systematic errors in T_{ci}^G.

    As expected from the results shown Fig. 5, there are significant changes in bias as a function of latitude for $T_{ci}^G - T_{DISK}$ (ranging from −50 K to 40 K) and $T_{ci}^G - T_{ci}^s$ (ranging from −145 K to −10 K). The good agreement with T_{MSIS} compared to the other variables is again apparent in Fig. 6 with an RMSD ranging from 60 K to 100 K (6–

275 18%) that is near the level of the random measurement uncertainty for a certain latitude and a negative temperature bias that gradually increases from 0 K in the southern high latitudes to −45 K (4–8%) in the northern high latitudes. It is not known at this time if this latitudinal trend in bias can be attributed to systematic measurement errors that change along the detector, biased altitude sampling of NRLMSISE-00 temperatures, and/or if NRLMSISE-00 is not completely capturing the latitudinal temperature gradient during this period. Further investigation is required to

280 reconcile such systematic biases between observations and models. For example, climatological comparisons of T_{ci}^G, T_{DISK}, T_{MSIS}, and T_{ci}^s along with TIMED GUVI derived temperatures over the full GOLD mission lifetime may likely shed light on this issue. This should be performed once version 3 of T_{DISK} is released which is expected to have significant improvements to version 2 used in this paper. Overall, the good agreement with T_{MSIS} over this time period demonstrates the validity in this two-channel ratio approach in probing thermospheric temperature using

285 LBH disk emissions.

4.3 Storm Time Response

    Figure 7 displays the response to a small geomagnetic storm in T_{ci}^G, Q_{JH}, $\rho_{SWARM}^{460\ km}$, and $\Sigma O/N_2^G$. The storm has started on 4 November 2018 and lasted to 5 November 2018 (Gan et al., 2020). T_{ci}^G, $\rho_{SWARM}^{460\ km}$, and $\Sigma O/N_2^G$ are

290 shown as percent differences from the quiet-time conditions on 2 November 2018. The global temporal evolution of

Atmospheric
Measurement
Techniques

Open Access

Discussions

EGU

these variables is in good agreement with each other and consistent with known storm time responses of thermospheric variables (e.g., Fuller–Rowell et al., 1994). A rise of magnetospheric energy influx as suggested by Q_{JH} leads to increased temperatures and upwelling of heavy molecular rich air in the high- and mid-latitudes as indicated by depletions of $\Sigma O/N_2^G$ (–40% near 50º latitude and –20% near –50º latitude) and enhancements of T_{ci}^G

295 (~20% near $\pm$50º latitude) and $\rho_{SWARM}^{460\ km}$ (~250% near $\pm$50º latitude). Enhancements of $\Sigma O/N_2^G$ (20–30% near 30º latitude) in the low-latitudes suggests a subsequent development of downwelling following the pole to equator global circulation in response to the storm-time Joule heating rise. Global thermospheric expansion is also apparent on November 5th as suggested by an increase of T_{ci}^G and $\rho_{SWARM}^{460\ km}$ over all latitudes. Note that the first detection of the temperature change was on the evening of 4 November when Joule heating rates have started to increase but are still

300 relatively low (< 50 GW). The post-storm recovery times are also in good agreement and appear to be on the order of 2–3 days.

5 Conclusions

A new technique to derive thermospheric temperature from space-based disk observations of FUV airglow

305 is presented. The technique uses a ratio of the emissions in two spectral channels that together span the Lyman–Birge–Hopfield (LBH) (2,0) band to determine the change in band shape with respect to a change in the rotational temperature of N_2. The definition of column-integrated thermospheric temperatures and other parameters used for comparison in the paper is given in Table 1. Specific findings of this work are as follows.

The LBH temperature signal is quantified with PCA of synthetic daytime LBH disk emission data to be just

310 3% of the intensity of an LBH band and accounts for just 1.6% of the total variability in the simulated LBH disk emissions. The PCA result underscores the difficulty in extracting the thermospheric temperature signal from LBH disk emissions and the necessity of denoising efforts to improve the SNR. Analysis of the secondary principal component mode, that characterizes how the LBH temperature signal manifests as the change in band shape, substantiates the approach to bin a LBH spectral band into two channels such that the temperature-induced band

315 shape change is best preserved. The SNR of the temperature signal is improved with the two channels compared to a fully resolved band. The study has shown that thermospheric temperatures can be derived from an observed two-channel ratio by using a precomputed relationship of the ratio to temperature from an LBH vibrational-rotational band model. In this two-channel ratio approach, representativeness errors originating from forward modeling are effectively eliminated because absolute LBH band intensities are not required in the derivation procedure, and

320 negative impact of systematic measurement errors, stemming from variations across the band system in the instrument's wavelength registration and resolution, is reduced because a fully resolved LBH band system is not required.

The derived temperature from the two-channel approach can have significant systematic biases of about 50 K (5–10%) if the wavelength registration and resolution are not known to the hundredth of a nanometer level and

325 tenth of a nanometer level, respectively, as shown in Fig. 3. In addition to these known sources of systematic biases, there is intrinsic random error in T_{ci} from shot noise. This shot noise is estimated to be 50–95 K (5–15%) for the

case of GOLD L1C data using MC simulations considering the viewing conditions and instrument performance as shown as gray dash line in Fig. 6.

330   The derived temperature is, in general, a column-integrated property referred to as column-integrated thermospheric temperature, T_{ci}. T_{ci} should not be attributed to the peak of the LBH contribution function without consideration of SZA and T_{ci} derivation uncertainty. This is particularly true for low SZA, where the observed LBH emissions emanate from a region of sharp temperature gradients. Using a priori knowledge of the thermospheric temperature profile from WAM simulations, as shown in Section 3.2, T_{ci}^s matches most to temperatures at altitudes 5–10 km higher (about 30–90 K hotter) than at $z_{\tau=1}$ for low SZA. As SZA increases, the gap between T_{ci}^s and

335   temperature at $z_{\tau=1}$ becomes smaller.

In a case study for the period of 2–8 November 2018 during which a small geomagnetic storm has occurred, T_{ci} agrees with T_{MSIS} across the disk with a bias that spans from 0 to -45 K with latitude and to a lesser degree with GOLD Level 2 temperature product. At low latitudes T_{ci}^G agrees well with T_{DISK}, T_{ci}^s, and T_{MSIS} with a consistent mean-bias-difference of about –25 K. Mean-bias and root-mean-squared differences between $T_{ci}^G - T_{DISK}$

340   and $T_{ci}^G - T_{ci}^s$ vary with latitudes as well as geomagnetic activity levels. The temporal evolution of global T_{ci} corroborates well with temporal changes of hemispherically integrated Joule heating rates Q_{JH}, SWARM mass density at 460 km $\rho_{SWARM}^{460\,km}$, and GOLD $\Sigma O/N_2^G$, which is consistent with known storm time responses of thermospheric variables.

345   **Data Availability**

The derived column-integrated temperatures for the period of November 2–8, 2018 using the procedure presented in this paper are available at https://doi.org/10.17605/OSF.IO/KHNQ7. GOLD L1C and L2 data can be accessed at the GOLD Science Data Center (http://gold.cs.ucf.edu/search/) and at NASA's Space Physics Data Facility (https://spdf.gsfc.nasa.gov). The code for NOAA's WAM model is available at https://github.com/NOAA-

350   SWPC/WAM. The code for the NRLMSISE-00 neutral atmosphere model is available from the NASA CCMC, at ftp://hanna.ccmc.gsfc.nasa.gov/pub/modelweb/atmospheric/msis/nrlmsise00/. The Python interface for the NRLMSISE-00 neutral atmosphere model is available at https://github.com/st-bender/pynrlmsise00. Near-Earth solar wind data is provided by the Goddard Space Flight Center Space Physics Data Facility and is available at https://omniweb.gsfc.nasa.gov/. The density measurements (L2 DNSxPOD data product) from Swarm can be

355   obtained through the web site at https://earth.esa.int/web/guest/swarm/data-access upon registration. AMGeO is an open source software available from amgeo.colorado.edu upon registration. SuperMAG ground magnetometer data is available at https://supermag.jhuapl.edu/. SuperDarn radar data is available at http://vt.superdarn.org.

Author Contribution

360   CC developed the presented technique and performed the analyses. TM contributed AMGeO, determined the validation approach and provided interpretation of the analyses. CC and TM prepared the manuscript.

Competing Interests

Atmospheric
Measurement
Techniques
Discussions

The authors declare that they have no conflict of interest.

365

References

Ajello, J. & Shemansky, Donald. (1985). A reexamination of important N 2 cross sections by electron impact with

395   application to the dayglow: The Lyman-Birge-Hopfield Band System and N I (119.99 nm). Journal of Geophysical Research. 90. 9845-9861. doi:10.1029/JA090iA10p09845.

Ajello, J. M., Evans, J. S., Veibell, V., Malone, C. P., Holsclaw, G. M., Hoskins, A. C., et al. (2020). The UV spectrum of the Lyman-Birge-Hopfield band system of N_2 induced by cascading from electron impact. *Journal of*

400   *Geophysical Research: Space Physics*, 125, e2019JA027546. https://doi.org/10.1029/2019JA027546

Akmaev, R. A. (2011). Whole atmosphere modeling: Connecting terrestrial and space weather, *Reviews of Geophysics*, 49, RG4004. doi:10.1029/2011RG000364.

405   Aksnes, A., Eastes, R., Budzien, S., and Dymond, K. (2006). Neutral temperatures in the lower thermosphere from N_2 Lyman-Birge-Hopfield (LBH) band profiles, *Geophysical Research Letters*, 33, L15103. doi:10.1029/2006GL026255.

AMGeO Collaboration (2019). A Collaborative Data Science Platform for the Geospace Community: Assimilative
410   Mapping of Geospace Observations (AMGeO) v1.0.0. Zenodo. http://doi.org/10.5281/zenodo.3564914.

Astafyeva, E., Zakharenkova, I., Huba, J. D., Doornbos, E., & van den Ijssel, J. (2017). Global Ionospheric and thermospheric effects of the June 2015 geomagnetic disturbances: Multi-instrumental observations and modeling. *Journal of Geophysical Research: Space Physics,* 122, 11, 716-11,742.
415   https://doi.org/10.1002/2017JA024174.

Budzien, S. A., Fortna, C. B., Dymond, K. F., Thonnard, S. E., Nicholas, A. C., McCoy, R. P., & Thomas, R. J. (2001). Thermospheric temperature derived from ARGOS observations of N_2 Lyman-Birge-Hopfield emission. 2001 AGUSM SA62A03B.
420

Cantrall, C. E., Matsuo, T., & Solomon, S. C. (2019). Upper atmosphere radiance data assimilation: A feasibility study for GOLD far ultraviolet observations. *Journal of Geophysical Research: Space Physics*, 124, 8154– 8164. https://doi.org/10.1029/2019JA026910.

425   Christensen, A. B., et al. (2003). Initial observations with the Global Ultraviolet Imager (GUVI) in the NASA TIMED satellite mission, *Journal of Geophysical Research: Space Physics*, 108, 1451, doi:10.1029/2003JA009918, A12.

Correira, J, Evans, J. S., Krywonos, A., Lumpe, J. D., Codrescu, M., Veibell, V., McClintock, B. E., & Eastes, R.
430   (2018). Global-scale Observations of Limb and Disk (GOLD): Overview of O/N_2 and QEV science data products. Abstract SA21A-3169 presented at 2018 AGU Fall Meeting, Washington, DC. 10–14 Dec.

Eastes, R. W. (2000a). Emissions from the N_2 Lyman-Birge-Hopfield bands in the Earth's atmosphere, *Physics and Chemistry of the Earth, Part C: Solar, Terrestrial & Planetary Science*, 25(5–6), 523– 527.
435   https://doi.org/10.1016/S1464-1917(00)00069-6.

Eastes, R. W. (2000b). Modeling the N$_2$ Lyman-Birge-Hopfield bands in the dayglow: Including radiative and collisional cascading between the singlet states, *Journal of Geophysical Research: Space Physics*, 105(A8), 18557–18573, doi:10.1029/1999JA000378.

440

Eastes, R.W., McClintock, W.E., Codrescu, M.V., Aksnes, A., Anderson, D.N., Andersson, L., et al. (2008). Global-Scale Observations of the Limb and Disk (GOLD): New Observing Capabilities for the Ionosphere-Thermosphere. In Midlatitude Ionospheric Dynamics and Disturbances (eds P.M. Kintner, A.J. Coster, T. Fuller-Rowell, A.J. Mannucci, M. Mendillo and R. Heelis). https://doi.org/10.1029/181GM29.

445

Eastes, R.W., McClintock, W.E., Burns, A.G. et al. (2017). The Global-Scale Observations of the Limb and Disk (GOLD) Mission. *Space Science Reviews* 212, 383–408. https://doi.org/10.1007/s11214-017-0392-2.

Fuller-Rowell, T. J., Codrescu, M. V., Moffett, R. J., and Quegan, S. (1994). Response of the thermosphere and
450   ionosphere to geomagnetic storms, *Journal of Geophysical Research*, 99(A3), 3893–3914, doi:10.1029/93JA02015.

Gan, Q., Eastes, R. W., Burns, A. G., Wang, W., Qian, L., Solomon, S. C., et al. (2020). First synoptic observations of geomagnetic storm effects on the global-scale OI 135.6-nm dayglow in the thermosphere by the GOLD mission. *Geophysical Research Letters*, 47, e2019GL085400. https://doi.org/10.1029/2019GL085400.

455

Laskar, F. I., Pedatella, N. M., Codrescu, M. V., Eastes, R. W., Evans, J. S., Burns, A. G., & McClintock, W. (2021). Impact of GOLD retrieved thermospheric temperatures on a whole atmosphere data assimilation model. *Journal of Geophysical Research: Space Physics*, 126, e2020JA028646. https://doi.org/10.1029/2020JA028646.

460   Matsuo T. (2020), Recent Progress on Inverse and Data Assimilation Procedure for High-Latitude Ionospheric Electrodynamics. In: Dunlop M., Lühr H. (eds) Ionospheric Multi-Spacecraft Analysis Tools. *ISSI Scientific Report Series*, vol 17. Springer, Cham. https://doi.org/10.1007/978-3-030-26732-2_10.

McClintock, W. E., Eastes, R. W., Hoskins, A. C., Siegmund, O. H. W., McPhate, J. B., Krywonos, A., et al.
465   (2020a). Global-scale observations of the limb and disk Mission implementation: 1. Instrument design and early flight performance. *Journal of Geophysical Research: Space Physics*, 125, e2020JA027797. https://doi.org/10.1029/2020JA027797.

McClintock, W. E., Eastes, R. W., Beland, S., Bryant, K. B., Burns, A. G., Correira, J., et al. (2020b). Global-scale
470   observations of the limb and disk mission implementation: 2. Observations, data pipeline, and level 1 data products. *Journal of Geophysical Research: Space Physics*, 125, e2020JA027809. https://doi.org/10.1029/2020JA027809.

Mende, S.B., Frey, H.U., Rider, K. et al. (2017). The Far Ultra-Violet Imager on the Icon Mission. *Space Science Reviews* 212, 655–696. https://doi.org/10.1007/s11214-017-0386-0.

475

Meier, R.R. (1991). Ultraviolet spectroscopy and remote sensing of the upper atmosphere. *Space Science Reviews* 58, 1–185. https://doi.org/10.1007/BF01206000.

Paxton, L.J., Morrison, D., Zhang, Y., Kil, H., Wolven, B., Ogorzalek, B.S., et al. (2002). Validation of remote

480   sensing products produced by the Special Sensor Ultraviolet Scanning Imager (SSUSI): a far UV-imaging spectrograph on DMSP F-16. *Proc. SPIE 4485, Optical Spectroscopic Techniques, Remote Sensing, and Instrumentation for Atmospheric and Space Research IV.* https://doi.org/10.1117/12.454268

Paxton, L. J., Schaefer, R. K., Zhang, Y., and Kil, H. (2017). Far ultraviolet instrument technology, *Journal of*

485   *Geophysical Research: Space Physics*, 122, 2706– 2733, doi:10.1002/2016JA023578.

Picone, J. M., Hedin, A. E., Drob, D. P., and Aikin, A. C. (2002). NRLMSISE-00 empirical model of the atmosphere: Statistical comparisons and scientific issues, *Journal of Geophysical Research: Space Physics*, 107(A12), 1468, doi:10.1029/2002JA009430.

490

Rodgers, C. D. (2000). Inverse methods for atmospheric sounding: Theory and practice. Singapore: World Scientific.

Solomon, S. C. (2017). Global modeling of thermospheric airglow in the far ultraviolet, *Journal of Geophysical*

495   *Research: Space Physics*, 122, 7834– 7848, doi:10.1002/2017JA024314.

Strickland, D. J., Evans, J. S., and Paxton, L. J. (1995). Satellite remote sensing of thermospheric O/N_2 and solar EUV: 1. Theory, *Journal of Geophysical Research: Space Physics,* 100(A7), 12217– 12226, doi:10.1029/95JA00574.

500

Visser, P., Doornbos, E., van den IJssel, J. et al. (2013). Thermospheric density and wind retrieval from Swarm observations. *Earth, Planets and Space* 65**,** 12 https://doi.org/10.5047/eps.2013.08.003.

Zhang, Y., Paxton, L. J., & Schaefer, R. K. (2019). Deriving thermospheric temperature from observations by the

505   global ultraviolet imager on the thermosphere ionosphere mesosphere energetics and dynamics satellite. *Journal of Geophysical Research: Space Physics*, 124, 5848– 5856. https://doi.org/10.1029/2018JA026379.

510

Tables and Figures

515

T_{ci}^{G}	Column-integrated thermospheric temperature derived from GOLD L1C disk data
T_{ci}^{s}	Column-integrated thermospheric temperature derived from simulated disk data
T_{DISK}	GOLD Level 2 version 2 thermosphere temperature product
T_{MSIS}	MSIS temperature at the altitude $z_{T_{ci}^{s}}$ (See Fig. 4)
Q_{JH}	AMGeO hemispherically integrated Joule heating rate
$\rho_{SWARM}^{460\ km}$	SWARM A mass density at 460 km
$\Sigma O/N_2^{G}$	GOLD Level 2 version 2 column O/N$_2$ ratio

Table 1: Definitions of symbols

520
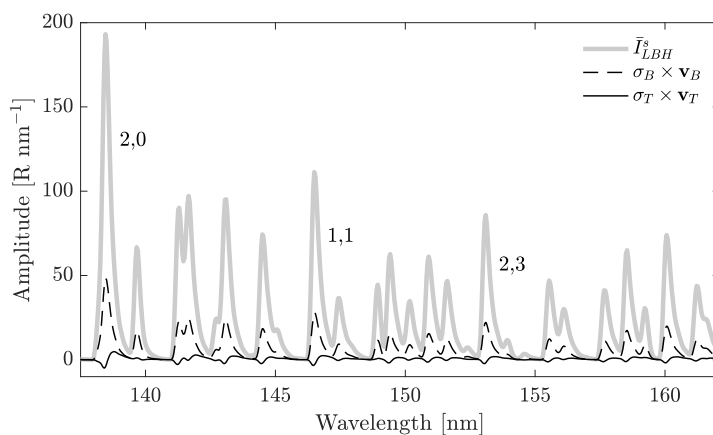
Figure 1: Simulated top-of-atmosphere mean LBH emissions (gray), $\overline{I_{LBH}^{s}}$, and the principal components associated with overall brightening of emissions (dashed black), v_B, and the temperature signal (solid black), v_T, scaled by their respective eigenvalues, σ_B and σ_T. These two principal components account for 99.9% of the variability about the mean. $\sigma_B{}^2$ accounts 98.3% of the total variability in the LBH emissions and $\sigma_T{}^2$ accounts for 1.6% of the total variability in the simulated LBH emissions over the entire disk over the period of November 2–8, 2018.

525
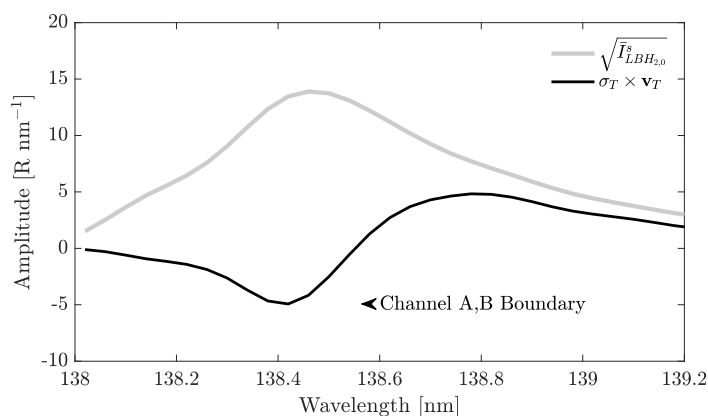
Figure 2: Principal component associated with temperature (black line), v_T, over the LBH (2,0) band scaled by the eigenvalue, σ_T. v_T represents an effective skewing of the emission feature to longer wavelengths or shorter wavelengths. Emissions at 135.56 nm, where v_T changes the sign, are unaffected by v_T (i.e., independent of temperature), and provide a boundary location to divide the (2,0) band into channels A and B. The shot noise level (gray) that is the dominant random noise source is also shown.
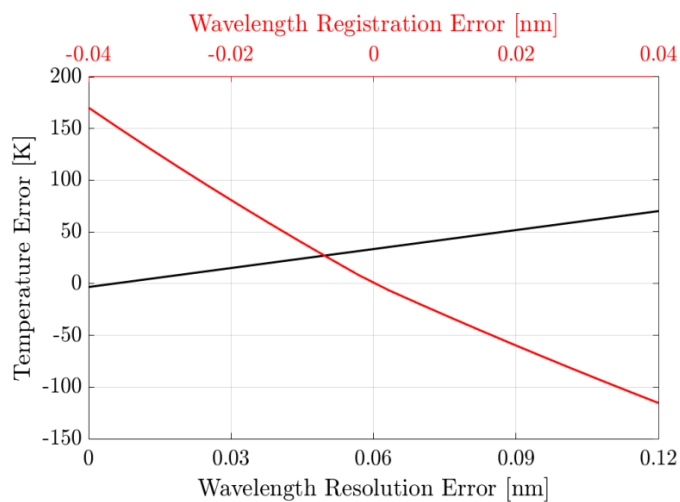

Figure 3: Expected bias errors in T_{ci} as a function of varying degrees of the two dominant known sources systematic measurement errors: the instrument's wavelength registration (red) and variations in the wavelength resolution (black).

16
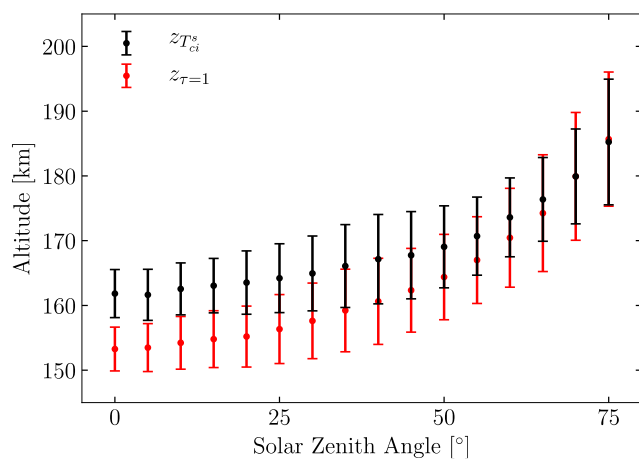
545   **Figure 4: The mean and standard deviation of the altitude of the simulated WAM temperature that is closest to T_{ci}^s , $z_{T_{ci}^s}$, as a function of SZA over the simulation period of November 2–8, 2018 (black). The mean and standard deviation of the peak of the LBH contribution function, $z_{\tau=1}$, is also shown as a function of SZA based on forward modeling of LBH disk emissions using the same WAM simulation (red).**
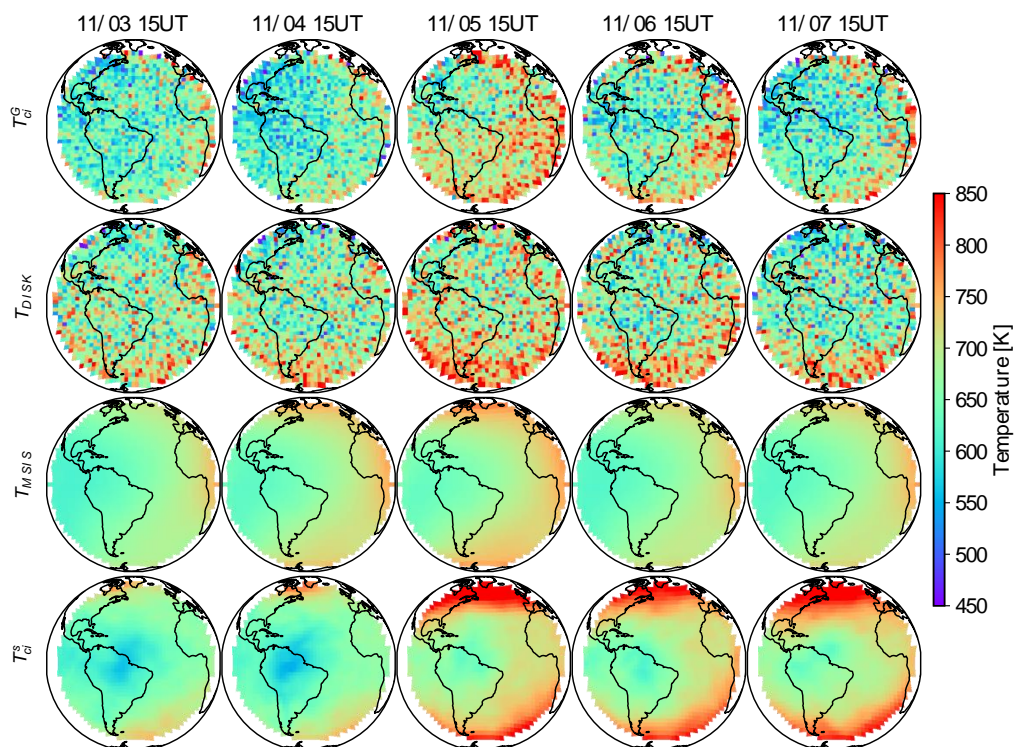
550

Figure 5: Comparison of T_{ci}^G with T_{DISK}, T_{MSIS}, and T_{ci}^S over Earth's disk viewed by GOLD for a five-day window from November 3-7, 2018 at about 15 UT, noon LT at the center of the disk (47.5ºW, 0ºN). A small geomagnetic storm has commenced the evening of November 4th and lasted through November 5th.
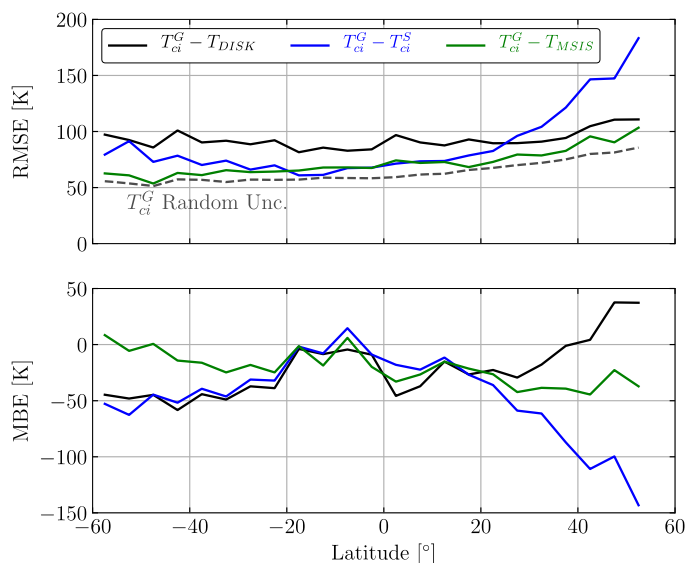
555

Figure 6: Root mean squared difference (top) and mean bias difference (bottom) of T_{ci}^G from T_{DISK}, T_{MSIS}, and T_{ci}^s computed for a given latitude over the period of November 2–8, 2018. The random uncertainty in T_{ci}^G is also shown by the gray dashed line (top).
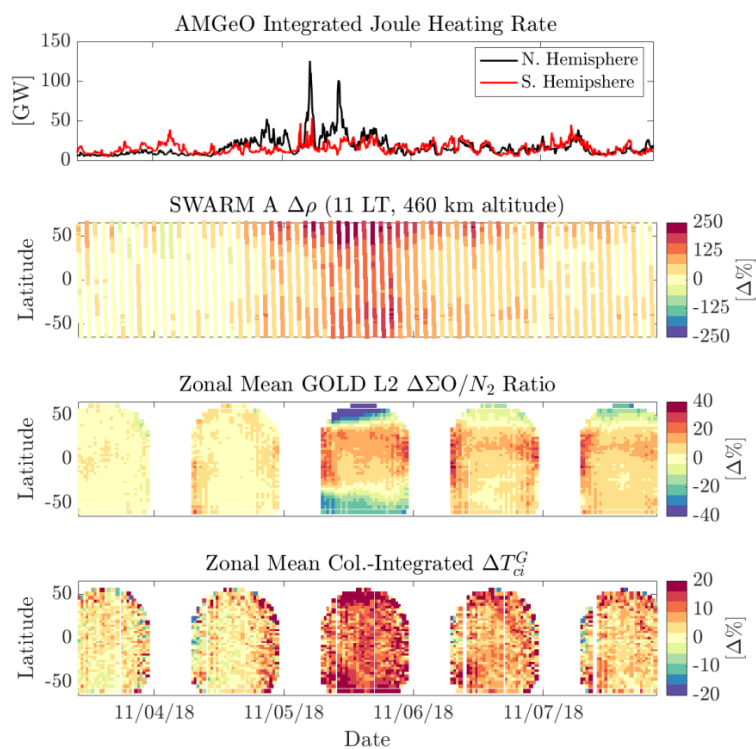
Figure 7: Storm-time response of the thermosphere as observed in three thermospheric variables as well as the hemispherically integrated Joule heating estimated using AMGeO. The percent change in mass density, ($\Delta\rho_{SWARM}^{460\,km}$), column O/N$_2$ ratio ($\Delta\Sigma$O/N$_2$), column-integrated temperature (ΔT_{ci}^{G}) are computed with quiet-time conditions on November 2nd, 2018.